EXPERIMENTS AND ANALYSIS OF EVAPORATION IN ELECTRODE PROCESSING FOR ENERGY STORAGE

A Thesis

by

MALCOLM THOMAS STEIN IV

Submitted to the Office of Graduate and Professional Studies of
Texas A&M University
in partial fulfillment of the requirements for the degree of

MASTER OF SCIENCE

Chair of Committee,	Partha P Mukherjee
Committee Members,	Hong Liang
	Philip Park
Head of Department,	Andreas A. Polycarpou

May 2015

Major Subject: Mechanical Engineering

ABSTRACT

Despite the wide range of ideal applications for LIBs, there is still room for improvement in their performance. While novel electrode materials are typically prohibitively expensive to develop and implement, changes to processing steps represent a cost-effective measure for improving the performance of LIBs that can be implemented almost immediately. Although each step of processing can impact the final microstructure of LIB electrodes, perhaps the most important step is the last: drying. This is when the final microstructure of the electrode is set. During this solvent evaporation stage, a non-uniform distribution of electrode constituents can develop in cases where the solvent evaporation rate exceeds that of the diffusion rate of the mobile electrode constituents. An even distribution of carbon black and binder throughout the electrode is crucial to ensuring the minimization of internal cell resistance, and therefore the maximum performance for a given electrode composition. In this work, we experimentally evaluate the impact of evaporation rate on the distribution of binder and carbon black in the electrode microstructure and the subsequent electrochemical performance.

Chapter I introduces some basic concepts in Lithium-ion batteries and a literature overview of related concepts. Chapter II details the experimental procedures and equipment utilized in this study. Chapter III details the results of experimental evaluation of evaporate rate and a 1-D analysis performed to determine the resulting particle distribution as a function of drying rate. Chapter IV details the post-processing

calendering used on electrodes and its result on electrode performance. Lastly, Chapter V details the summary and future outlook for this work.

My analysis has shown that a slower two-stage dry – as opposed to a high-rate single stage dry – allows for an optimal, more even volumetric distribution of binder and conductive additive, thus reducing cell resistance and improving electrochemical performance.

ACKNOWLEDGEMENTS

I would like to thank my committee chair, Dr. Partha Mukherjee, and my committee members, Dr. Hong Liang, and Dr. Philip Park for their guidance and support throughout the course of this research. I'd also like to thank Dr. Chris Rhodes, whose experimental guidance was invaluable.

Thanks go to my friends and colleagues and the department faculty and staff for their assistance over the last two year. I also want to thank my colleagues in the ETSL that have made my graduate experience memorable.

Finally, thanks to my family for their encouragement and Leeza for tolerating all my late night trips to the lab.

NOMENCLATURE

D_0	Diffusion constant (m^2/s)
$\dot{E}$	Rate of evaporation front reduction (m/s)
H	Initial film height (m)
k	Boltzman constant (J/K)
$K(\varphi)$	Sedimentation coefficient (-)
R	Particle/aggregate radius (m)
Pe	Peclet number ()
T	Temperature (K)
t	Time (s)
$\bar{t}$	Dimensionless time (s)
y	Vertical position in film (m)
$\bar{y}$	Dimensionless film position (-)
$Z(\varphi)$	Compressibility (-)
φ	Volume fraction (-)
φ_m	Upper limit on particle volume fraction (-)
φ_0	Initial volume fraction (-)

TABLE OF CONTENTS

LIST OF FIGURES

CHAPTER I

INTRODUCTION AND LITERATURE REVIEW

Increasing concerns about rising fuel prices, energy security, and climate change have given rise to interest in the adoption of renewable energy in place of traditional, petroleum-based fuels. The implementation and usage of renewable energies has been limited by a lack of effective storage and transportation mediums. Recent improvements in the energy density and durability of lithium-ion batteries (LIBs) have made them an increasingly attractive means of energy storage[1, 2, 3, 4]. Further improvements in lithium-ion technology would increase the viability of renewable energy sources and thus assist in their widespread adaptation. For example, improvements in the capacity of LIBs would not only improve the effective range of electric vehicles[5, 6], but also improve their cycle life by reducing the depth of discharge, which in turn increases the viability of LIBs for use in grid energy storage applications[7].

The performance of batteries, regardless of type, is dependent on the materials that form the positive and negative electrode, the choice of electrolyte, and the cell architecture[4, 8, 9, 10, 11, 12]. A typical LIB electrode is composed of a combination of Li-containing active material, conductive additive, polymeric binder, and void space that is filled with an electrolyte. Typically, these cathodes are created by casting out and drying a thin film of a slurry containing these components. A number of studies have analyzed the impact of microstructural characteristics such as electrode thickness[13, 14, 15, 16],

porosity[17], active material particle size[18, 19, 20, 21], conductive additives[22, 23, 24, 25, 26, 27], and general composition[28, 29], but little attention is paid to electrode processing.

Electrode processing can be broken up into five main sections: dry powder mixing, wet mixing, substrate preparation, film application, and drying. When producing an electrode using these processing steps, the goal up until drying is to achieve a uniform slurry consisting of the active material, conductive additive, binder, and solvent. This uniform distribution is critical to optimal performance of LIBs[30]. A number of methods are used to achieve a uniform dispersion of components up to this point, including hand grinding, sonification, vortexing, etc. However, these efforts can be undone by the redistribution of mobile components during solvent evaporation. Should this occur, the uneven distribution of additive and binder could increase/decrease the local porosity and local electrode conductivity, which could lead to an increase in internal resistance and a decrease in performance.

Drying of thin films has been an active field of study for over 40 years. However, the majority of the analysis has focused on the drying of colloidal suspensions such as latex films, with little or no studies focused on the impact of drying in battery electrodes. Many experimental studies neglect to even mention the type of drying utilized, or simply place their wet electrodes in an oven at high temperatures until dry[31, 32, 33, 34]. One study looked at the influence of solvent type (organic or aqueous) on the resulting microstructure as a result of the differing solvent evaporation rate[35]. Their study showed a direct correlation between the drying rate and the distribution of binder and conductive additive within the sheets. However, an apparent shortcoming of this study is the

thickness of the cells utilized (~1500 um) which is not realistic for most LIB applications. A recent study has demonstrated the impact of solvent evaporation rate on the favorable aggregation of conductive additives, but is lacking in terms of an experimental counterpart[36].

In thin film drying theory, three stages of the drying process exist[35, 37, 38, 39, 40, 41]. Initially the particles are suspended in an ample amount of solvent, such that the solvent on the surface evaporates at an increasing rate until the top layer of liquid is gone. Following this stage, the solvent evaporating from the surface has to come from within the sheet. Thus solvent must migrate from the interior of the sheet to the top. This process occurs until the structure is consolidated, whereby a wetted solid structure exists where the particles have formed a 3D inter-connected network with solvent contained in the porous space. During the final stage of drying the structure no longer shrinks, with the remaining solvent diffusing to the surface of the sheet.

Beyond the basic mechanics of thin film drying, there are additionally three distinct drying modes that have been observed[42]. In the first mode, the distribution of particles and solvent is homogenous, and every part of the thin film dries at the same rate. In the second mode, the vertical accumulation of particles occurs due to poor particle diffusivity[43]. A sheet of particles forms at the surface of the sheet and increases in thickness as the solvent evaporates. This involves a competition between an evaporative time scale and a diffusive time scale. The ratio of the diffusive time scale to the evaporative time scale can be expressed as the Peclet number:

$$Pe = \frac{6\pi\mu R_0 H\dot{E}}{kT} \quad (1)$$

where R_0 is the particle/aggregate radius, μ is the viscosity of the solvent (kg/(m*s), H is the initial film height, $\dot{E}$ is the rate of evaporation front reduction (m/s), k is the Boltzman constant (J/K) and T is the temperature (K). Here, a value less than 1 indicates that vertical accumulation is less likely, with a value greater than one indicating a higher degree of vertical accumulation.

Lastly, the third mode consists of the migration of a horizontal drying front across the surface of the drying film[44, 45]. Here drying begins at the edges of the sheet and propagates inward, potentially resulting in "coffee ring" formations, whereby particles accumulate at the edges of the drying front. In practice, a combination of the latter two methods is commonly observed.

In this study, the effect of evaporation on microstructural formation and resulting electrochemical performance is evaluated. This determined via direct experimentation with the construction and electrochemical analysis of coin cells. Additionally, a 1-D model will be incorporated to elucidate the results of the study.

CHAPTER II

NON-AQUEOUS PROCESSING IN LIBS

Research into new and improved materials to be utilized in Lithium-Ion batteries necessitates an experimental counterpart to any computational analysis. Testing of Lithium-Ion batteries in an academic setting has taken on several forms, but the at the most basic level is the coin cell. Originally used for hearing aids in the 1950's, today coin cells are commonly used in the development and evaluation of new and existing electrode materials. As one of the smallest form factors for batteries, these cells represent a simple and effective way to create batteries in an academic research setting. This chapter represents the steps partially developed by myself and utilized in the ETSL to manufacture coin cells for the evaluation of new and existing electrode materials. All equipment was selected by myself.

Experimental Equipment

Electrode processing can be broken up into five main sections: dry powder mixing, wet mixing, substrate preparation, film application, and drying, as illustrated in Figure 1.

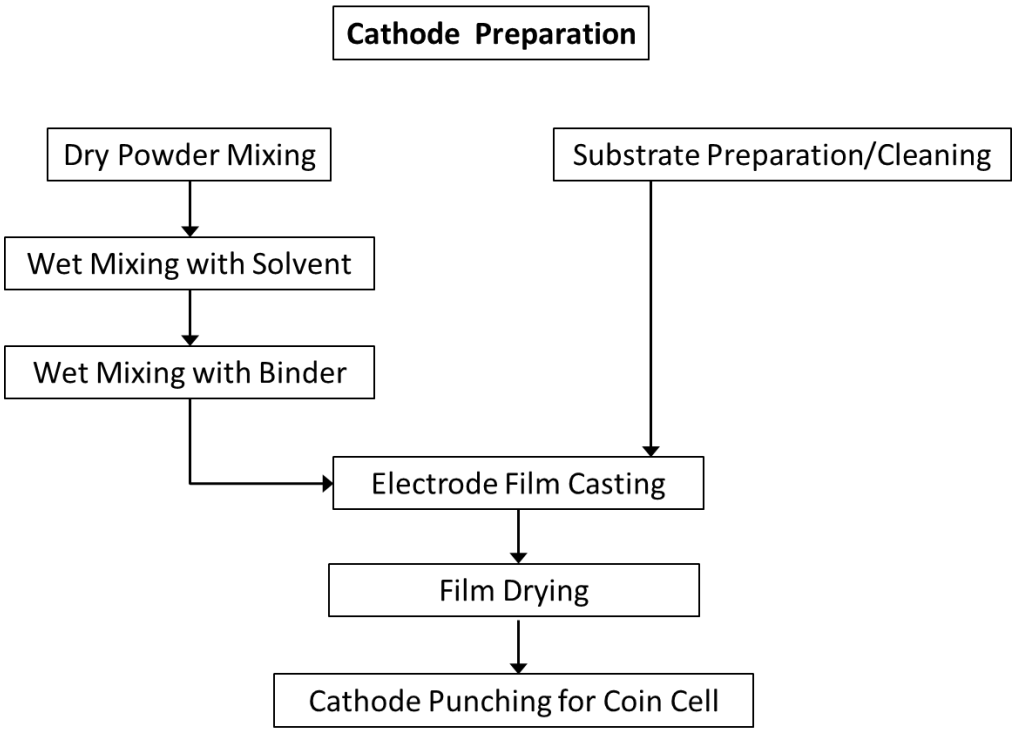

Figure 1. Schematic overview of the steps utilized in the ETSL to create cathodes.

The equipment and preparation stations utilized in this study are presented herein. A visual overview of the ETSL experimental facility can be seen in Figure 2.

Figure 2. Panoramic view of ETSL experimental laboratory.

The electrode substrate and slurry preparation station is shown in Figure 3. The IKA tube mixer pictured ensures the uniform dispersion of the electrode components (active material, conductive additive, and binder) within the slurry.

Figure 3. Electrode substrate and slurry preparation station.

The binder preparation and dry powder mixing station is shown in Figure 4. The high accuracy of the Ohaus scale ensures accurate and high precision measurements for the determination of critical electrode properties, such as specific capacity. The digital micrometer (in case) allows for the determination of film thicknesses in increments of 0.001 mm.

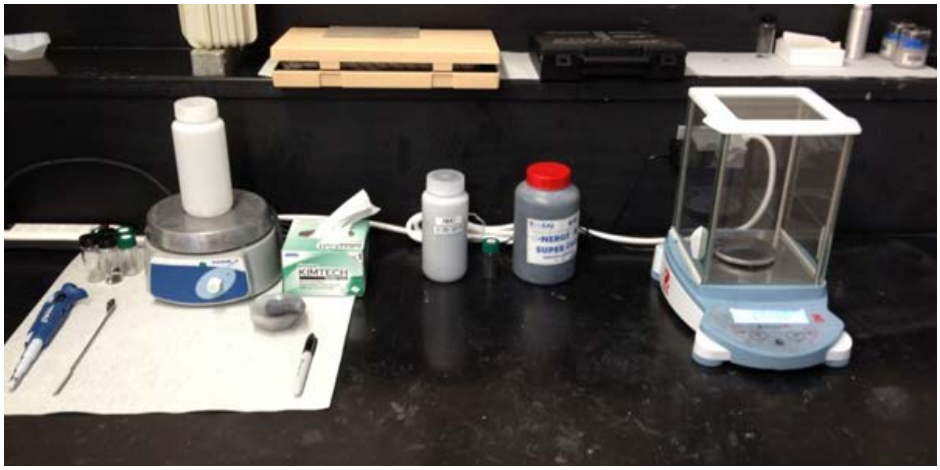

Figure 4. Binder preparation and dry powder mixing station.

The vacuum oven and film applicator are pictured in Figure 5.

Figure 5. MTI vacuum oven and Elcometer film applicator.

The vacuum oven is capable of reaching temperatures up to 250^{o}C with a pressure range of -0.1 Mpa~0 Mpa (atmospheric pressure). The oven allows for quick second-stage drying of electrode sheets, while also removing any bubbles present in the electrode

sheet surface. The film applicator (used in conjunction with the pictured doctor blade) ensure a smooth, even electrode casting. 11 preset traverse speeds are available, from 0.5-10cm per second. Lastly, our coin cell crimper is pictured in Figure 6 within our glovebox. The glovebox has a pure argon environment with O_2 and H_2O levels maintained below 0.5 ppm at all times. The crimper (which seals coin cells) can be used on CR2032, CR2025, and CR2016 coin cells.

Figure 6. Coin cell crimper pictured within glovebox.

After finalizing the construction of the coin cells, they are electrochemically characterized via the usage of the ARBIN BT2000 and VMP3 systems shown in Figure 7.

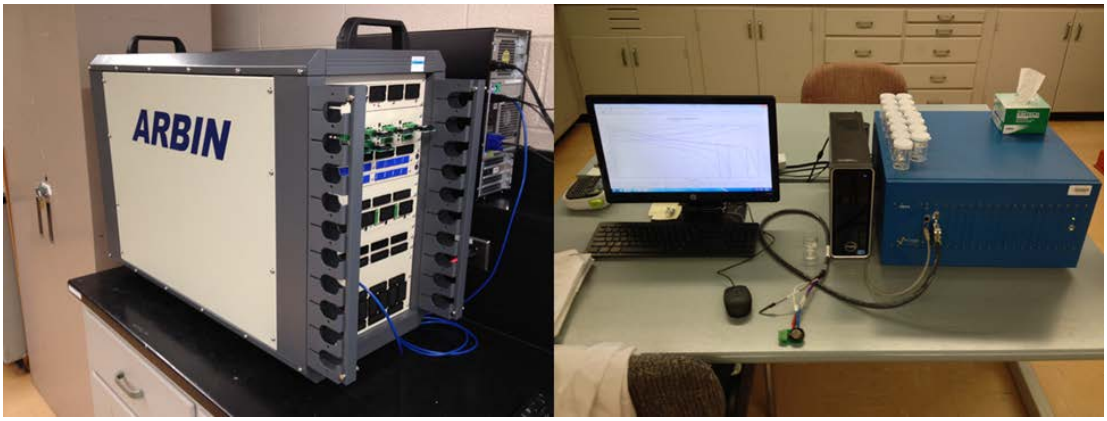

Figure 7. Arbin BT2000 battery cycler and Biologic VMP3 with Potentiostat/Galvanostat/EIS capabilities.

Materials

$LiNi_{1/3}Mn_{1/3}Co_{1/3}$ with an average particle size of 8-12 μm, BET surface area of 0.3-0.8 m^2/g, and a density of 2.2 g/cm^3 was acquired from Targray. The manufacturer suggested specific capacity is 155 mAh/g when cycled at 0.2C between 4.2-2.7 V. In practice, the highest achievable specific capacity corresponded to 145 mAh/g when cycled at 0.1C. Super C-65 (carbon black) with an aggregate size <1 um, BET surface area of 62.4 m^2/g, and a density of 160 kg/m^3 was acquired from TIMCAL. Kynar Flex 2801 PVDF was supplied by Arkema, and 1.0 M $LiPF_6$ in EC/DEC (1:1 by vol) was purchased from BASF. Anhydrous N-methylpyrrolidone (NMP) with less than 0.005% water content was purchased from Sigma-Aldrich. Lithium ribbon was obtained from Sigma-Adlrich.

Cathode and Coin Cell Preparation

In this case the desired composition of the dried electrode is to be 70% NMC, 20% Super C-65, and 10% PVDF. This composition is chosen to achieve discharge of cells at higher rates, but other compositions have been reported as well[31, 46, 47, 48, 49, 50]. Thus the preparation steps will use the appropriate quantities needed to create the desired [51]sheet. During the initial stage, 1.25 g of NMC and 0.25 g of Super C-65 are measured out and mixed in a mortar and pestle. This step serves to break up any large aggregates of active material or conductive additive and ensure that the active material and additive are uniformly mixed prior to wet mixing. The pre and post mixed samples can be seen in Figure 8.

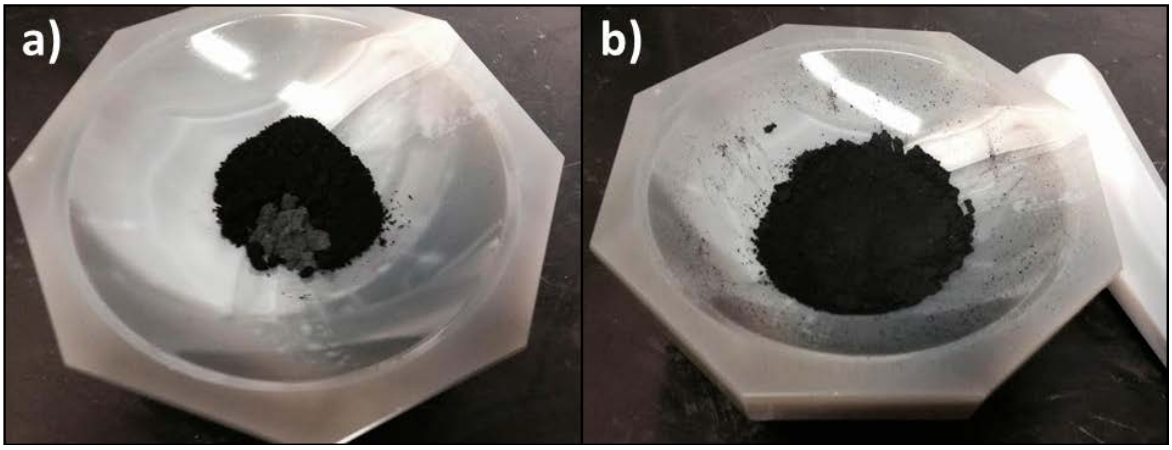

Figure 8. Pre (a) and post-mixed (b) NMC and Super C-65.

During the second stage, the mixed powder is placed into an IKA Tube mixer with 5.5 ml of NMP and 16 6mm diameter glass balls. The minimum quantity of glass balls needed is dependent on the mixing ability of the components within the vial.

However, an upper limit exists due to the loss of slurry coating the glass balls after mixing. With too little slurry or too many balls, it will not be possible to extract enough of the electrode slurry to cast an electrode. In practice, 16 balls is sufficient to achieve a uniform dispersion and allow for more than sufficient slurry amount for casting. The amount of NMP required is based on the total surface area of the particles present in the dry mixture. For example, if the desired dry weight ratio of components was adjusted to include 10% Super C-65 as opposed to 20% (with 80% NMC and 10% PVDF), a significantly lower amount of NMP would be required: approximately 2.0 ml. Thus the determination of the appropriate solvent content in the initial mixing stage must be carefully determined when working with new desired sheet compositions. The slurry is then allowed to mix on the max setting until uniform, which corresponds to approximately 15 minutes. 1.25 g of a 10% PVDF by weight in NMP solution is then added to the tube, and allowed to mix for 5 more minutes. The mixing slurry can be seen in Figure 9.

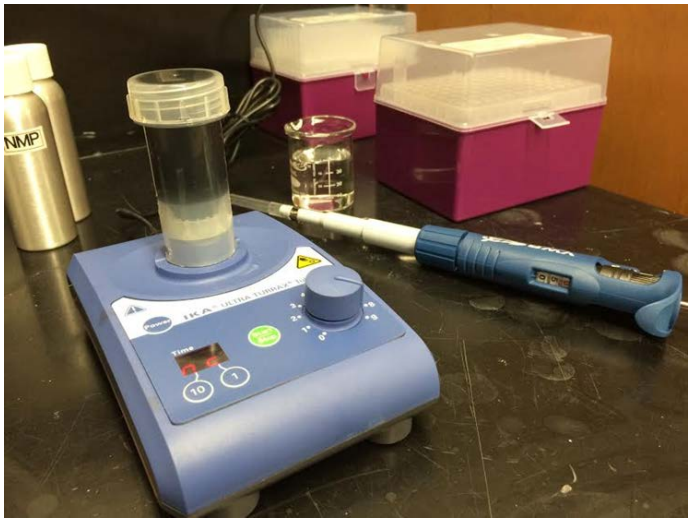

Figure 9. Electrode slurry mixing on IKA mixer. A two-stage mix is utilized, where the solvent is mixed with the dry powder, and is again mixed after adding the 10% by weight binder solution.

During the mixing stages, the electrode substrate is prepared. An aluminum substrate is used for cathodes, and a copper substrate is used for anodes. As the cathode is the focus of this study, the aluminum foil will be used as the substrate. During the manufacturing process, the aluminum foil is coated with a thin layer of oil to prevent self-adhesion when rolling the material. Thus prior to casting, the substrate must be cleaned. Here a rough scotch pad is used to physically etch the surface of the sheet, with acetone applied to the surface of the sheet. During the physical etching, the surface is roughened, allowing for greater electrode adhesion. The acetone serves to remove the oil from the surface alongside the physical etching. During etching, acetone is sprayed onto the surface of the sheet, and the sheet is etched using small circular patterns across the sheet. Acetone is routinely sprayed on the surface to keep it coated, and the sheet is

wiped with a paper towel as required to remove residue from the surface, as shown in Figure 10.

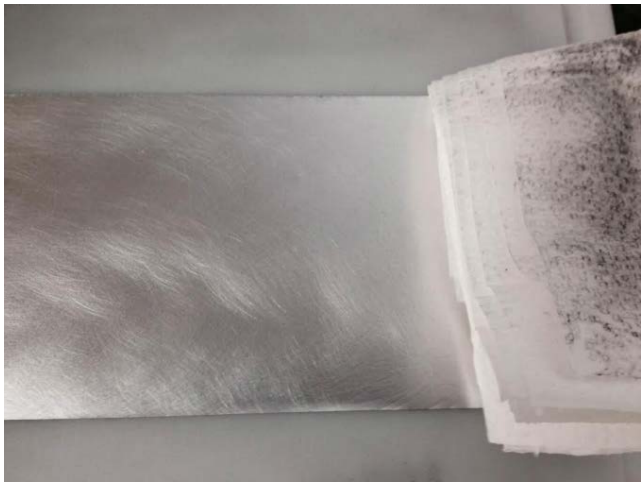

Figure 10. Cleaned aluminum substrate with residue shown on paper towel.

After etching both sides, the sheet is rinsed with D. I. water and isopropyl alcohol. If the water slides off of the sheet without beading, it is sufficiently oil-free such that the electrode slurry will adhere to the current collector well. If the water starts to bead, the sheet needs to be recleaned.

After allowing the substrate to dry and the electrode slurry has finished mixing, the electrode is cast. It is important to proceed directly to casting after mixing the electrode slurry to prevent any potential settling of the slurry components (primarily the active material). If for some reason the slurry is left sitting for more than 5 minutes, it is remixed for another 15 minutes. The current collector must first be applied to the surface of the film applicator. To do this, a layer of isopropyl alcohol is sprayed on the surface,

and the electrode sheet is placed on top with the duller side face up. A paper towel is then used to flatten the foil such that it is completely flush with the applicator. After placing the foil, the slurry is ready to be poured onto the surface of the current collector. The slurry should be poured in a three inch line across the width of the sheet, 1 inch from the top, as shown below. It is not uncommon for the glass mixing balls to fall out of the vial onto the sheet. In this case the balls may simply be picked out with cleaned tweezers. To cast the slurry, an Elcometer film applicator and doctor blade are utilized. The film applicator has a mechanical arm that can be controlled to move forward at a desired rate. The doctor blade consists of an adjustable gap that allows slurry to pass through when slid over a surface. Thus as the mechanical arm pushes forward, it additionally pushes the doctor blade forward, leaving a cast electrode in its wake, as shown in Figure 11.

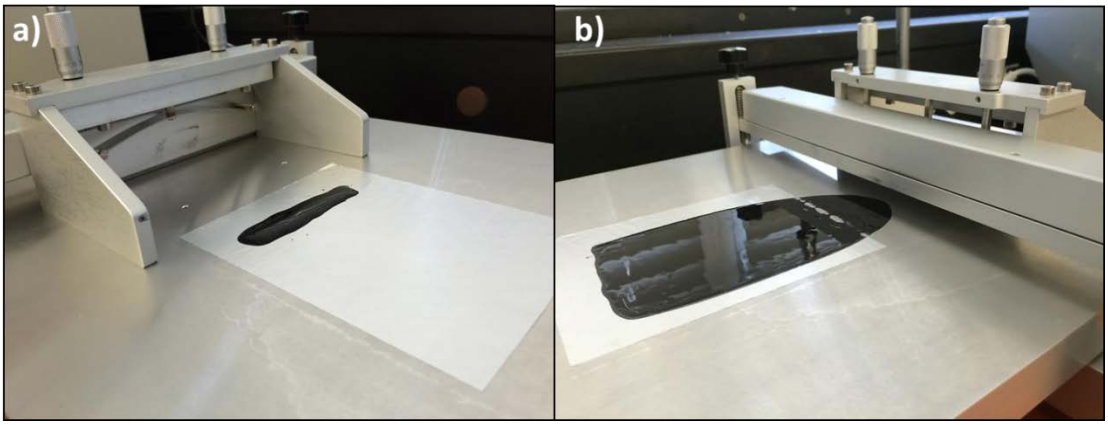

Figure 11. Electrode slurry poured onto aluminum substrate before (a) and after casting (b).

The height of the doctor blade is set at 200 µm. After casting, the sheet is labeled and lifted from the surface of the applicator with a sheet of cardboard to prevent excessive bending of the cast electrode. Typically small bubbles will appear on the surface of the sheet, which are simply allowed to pop on their own. The electrode sheet can be dried in a number of ways, ranging from air dry to oven dry, or a combination of both methods. A common method reported in the literature is to simply place the wet electrode sheet into an oven at 120^{o}C until dry.

After the cast electrode is dried, the quality of the sheet can be determined. A good sheet should have a uniform surface appearance and adhere to the current collector well. Sheet uniformity can be visually inspected, and adhesion can be tested by passing a spatula over the surface of the sheet and rolling the sheet around a pencil. If no flaking occurs in either step the electrode adhesion is typically sufficient. Typically flaking of the electrode sheet is caused by either poor etching of the substrate, or having to little NMP in the initial mixing stage. Alternatively, too much NMP can cause the sheet to display a higher degree of porosity, which is not desirable. Thus it is important to optimize the NMP content for each slurry composition. Lastly, a third pattern can be observed on the electrode surface, where pooling appears to occur. Interactions with the ambient conditions of the room (humidity, temperature, and any air movement) are the most likely causes for this behavior. By isolating the electrode sheet in the vacuum oven (whether drying at room temperature or at an elevated temperature) this pattern can be prevented. These scenarios are displayed in Figure 12.

Figure 12. Electrode sheets: a) with too little NMP, b) with too much NMP, and c) with non-uniform drying.

After confirming the quality of the electrode sheet, electrodes can be punched from the sheet. Here a ½" hole punch is used to punch out the cathodes on top of an aluminum plate. A hard surface is needed to ensure that the cathode edges do not curl up whilst being cut. However, the metal must also be soft enough such that the edges of the punch are not dulled excessively. A punched out electrode can be seen in Figure 13.

Figure 13. Electrode sheet shown with punched out cathode.

After punching the electrodes, the cells need to be further dried in a vacuum oven at 120^{o}C overnight. The electrodes are then weighed and transferred directly to the glovebox antechamber. When transferring any items into the glovebox, the antechamber must be purged of any oxygen. Thus the vacuum is brought down to -1 bar, and then filled with Argon. This process is then repeated 1-2 more times, depending on the samples transported into the glovebox. A number of items necessary for making coin cells, including the electrolyte, separators, lithium ribbon, and coin cell crimper are already in the glovebox. Within the glovebox, the coin cell is then assembled. Before assembling the coin cell, the lithium counter electrode needs to be prepared. This counter-electrode consists of a cut disk of cleaned lithium stuck to the surface of a 0.5 mm stainless steel spacer. To clean the lithium, a small portion of lithium is unrolled and a razor blade is used to scrape off the outer surface that has oxidized. A disc of lithium is then punched out using a hold punch, and is then pressed onto the surface of the separator. Small notches can be applied to the disc to improve adhesion if necessary. Typically this is necessary when excessive force is used whilst cleaning. This and the necessary components to make the coin cell can then be placed in a weigh boat.

Moving on to cell construction, first the cathode is centered in the coin cell case. After, several drops of electrolyte are applied to the electrode surface. Enough electrolyte should be applied such that the electrode surface is wetted and a ring of electrolyte can be observed on the outer edge of the coin cell case. Then a single ¾” diameter separator is applied to the surface. Care must be taken to center the electrode and prevent bubbles from forming under the separator. Any bubbles that do become

trapped can be forced out using the flat edge of a pair of tweezers. If the electrode moves out of the center, the case can be grabbed by the lip and lightly tapped to force the electrode into position. An additional drop or two of electrolyte can be applied to allow for better movement of the electrode if it sticks to its original position. Next, the gasket is placed into the cell. After applying a few more drops of electrolyte, the lithium counter electrode may be placed, along with the wave spring. The cell is then filled to the brim with electrolyte and the cap is carefully placed on top. Care must be taken to avoid excessive loss of electrolyte. The cap can then be pressed down using a thumb, and then transported to the crimper using tweezers. After sitting the cell in the grooves of the crimpers, the pressure can be applied up to 900-1000 psi and then released. The cell should appear as shown in Figure 14, with no broken edges. An additional schematic of the placement of the cell components can be seen in Figure 15.

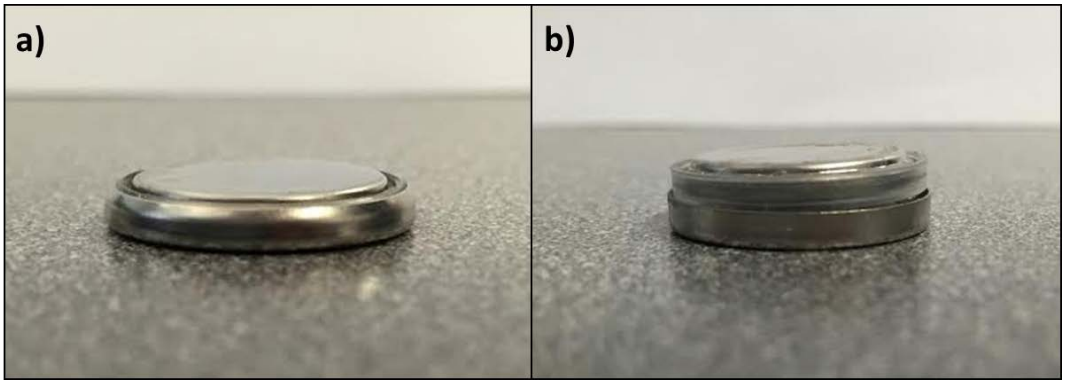

Figure 14. Coin cell that has been (a) properly crimped and (b) improperly crimped.

When the cell is not properly sealed, exposure to the atmosphere will cause swelling of the lithium, which will cause the cell to expand and pop open.

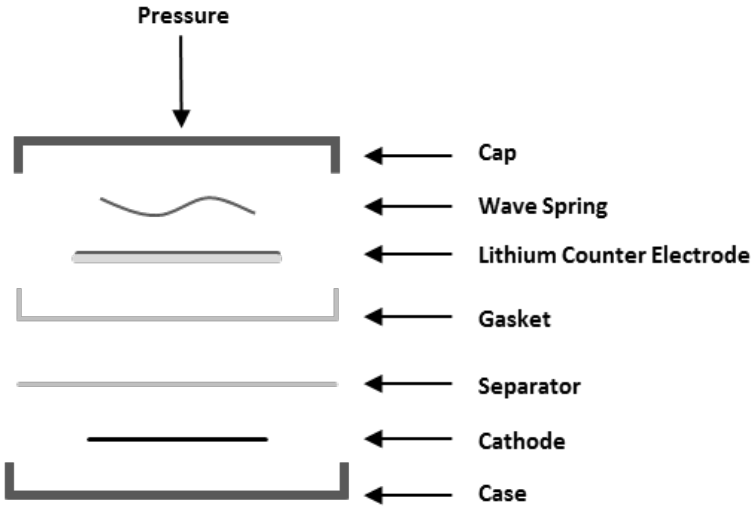

Figure 15. Coin cell components displayed in order of placement within cell.

After the cell is crimped and transported out of the glovebox, it is ready to begin cycling. The cells are subjected to cycling between 4.2V and 2.8V at several rates. In order to cycle the cells, the C-rate must be determined. C-rate is the standard used to determine speed at which a cell is charged or discharged. At a rate of 1C, the applied current will be such that the cell is charged or discharged in 1 hour. A rate of 5C means 1/5th of an hour, and a rate of C/5 would mean 5 hours. The specific capacity of the active material is given by the manufacturer as 155 mAh/g. Thus to determine the C-rate it is necessary to know the mass of active material in the completed electrode. With the weight of the foil known, this can be determined by simply subtracting the foil weight from the measured electrode mass and multiplying by the weight percentage of active material in the electrode. After acquiring this number, the cell can be cycled as shown in Figure 16.

Figure 16. Coin cells undergoing cycling (charge/discharge at different rates) on the Arbin system.

CHAPTER III

EFFECT OF EVAPORATION

The distribution of mobile electrode constituents after drying has a significant impact on the final electrode microstructure. The distribution of conductive additive and binder influences the electrical conductivity, porosity, and tortuosity of an electrode[28]. Both electron transfer from the current collectors through the electrode and charge transfer at the surface of active material particles can be detrimentally impacted by an uneven distribution. Although short range conduction can be improved in some areas with higher concentrations of additive, a tradeoff exists between electrical conductivity and resistance to ion transfer: as more material is present (via reduced porosity), the amount of space available for ion transport is reduced, thereby increasing the difficulty of ion transport and impacting the power and performance capability of LIBs[52, 53, 54]. Microstructure and cell performance are probed to determine the impact of evaporation rate on particle distribution, and a 1-D model is adapted to elucidate the theoretical distribution with the electrodes.

Electrode Drying

In the penultimate processing stage the wet electrode film is dried. Both a single stage and two-stage drying approach was utilized. One sheet was immediately placed into a vac-uum oven (at atmospheric pressure) at 120^{o}C for 1.5 hours, with the weight of the electrode sheet being measured every 15 minutes. The other sheet was allowed to dry at room temperature overnight. The electrode sheet was weighed directly after casting,

and after the 16 hour room tempera-ture dry. After this first step, the surface of the electrode sheet is still wet. Thus a second drying stage is utilized, where the sheet is placed into the vacuum oven at 70^{o}C for 3 hours (or until dry), with the weight again being measured every 15 minutes. The weights of the electrode sheet were plotted as a percentage of the original electrode weight, before drying began. Thus the weight percent losses indicate the amount of solvent evaporating over time. The plots of the weight loss as a function of time for the sheets can be seen below in Figure 17.

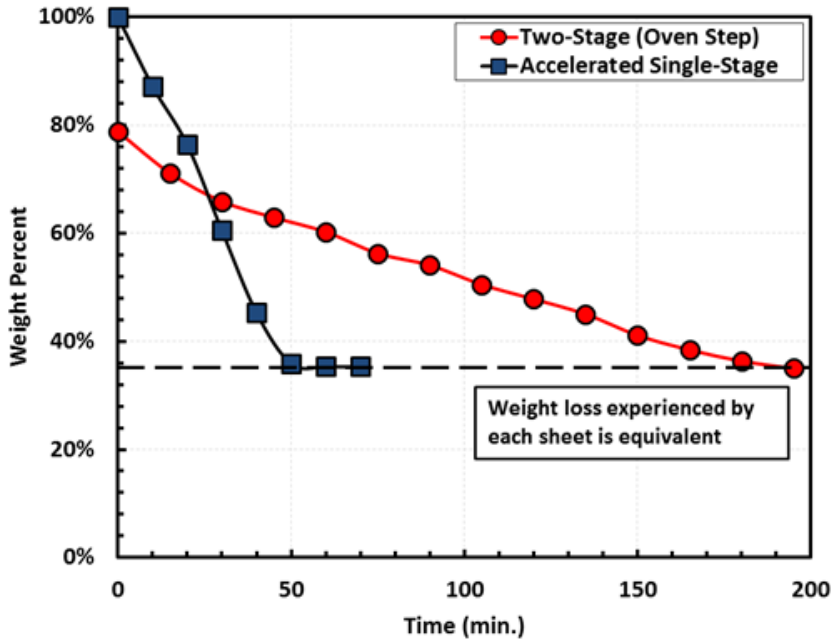

Figure 17. Comparison of total electrode sheet weights as a function of time for the oven drying stages.

Here, the initial drying stage for the slower case has already occurred. Thus this case starts at 80%. The slope for the accelerated single-stage sheet is higher than that of the

second stage of the two-stage sheet, indicating a higher rate of solvent evaporation. As expected, the loss percentage for each sheet becomes equivalent at the termination of drying.

Microstructural Analysis

Given the thin nature of the electrode sheets used in this study, separation of the electrode into multiple layers for local volume fraction analysis was not feasible. Although thicker electrode sheets could be utilized, efforts were taken to reduce any changes to drying dynamics that would be observed in LIB electrodes of typical thickness[32]. A number of advancements in electrode microstructure imaging exist such as XRT which allows for complete digital electrode reconstruction, but this detailed analysis is beyond the scope of this paper[55, 56, 57, 58]. However, the top and bottom surfaces of the electrode can be observed to give insight into the distribution of mobile components within the electrode. SEM images of the upper surface of the punched out electrodes can be seen in Figure 18.

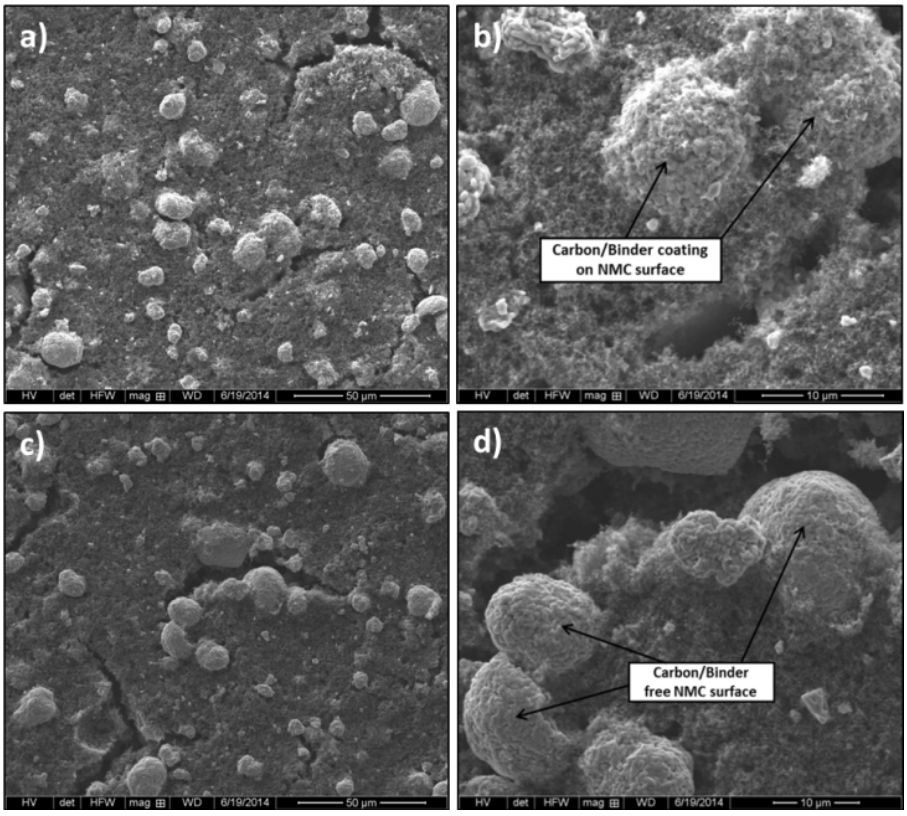

Figure 18. SEM images of a) Two-stage dried electrode sheet zoomed out with 50µm scale, b) Two-stage electrode sheet zoomed in with 10µm scale, c) Accelerated single-stage electrode sheet zoomed out with 50µm scale, and d) Accelerated single-stage electrode sheet zoomed in with 10µm scale.

Immediately noticeable when comparing the two cases is the presence of a binder/additive coating on the surface of the two-stage electrode that is not present for the single-stage case. This initially indicates the presence of additional binder on the surface of the two-stage sheet, as compared to the single-stage sheet. However, if we assume the migration of additive with the binder, particle interactions in terms of surface area adhesion would likely restrict the ability of the binder to coat the active material. Thus assuming that vertical accumulation of binder and additive occurs not during the

two-stage, but during the single stage dry, it is likely that the additional binder and additive at the surface would cause local competition between the active material and additive with binder adhesion[28, 59]. Thus there is not enough binder to form fixed layers on the surface of the active material particles, limiting potential contact area between the conductive network and the active material particles. With the additional binder/additive on the surface of the electrode sheet, a gradient will have developed within the sheet, whereby a lower weight percentage of binder/additive will exist towards the bottom of the electrode. To verify that vertical accumulation is indeed occurring, SEM images of the bottom of the electrodes were examined, as shown in Figure 19.

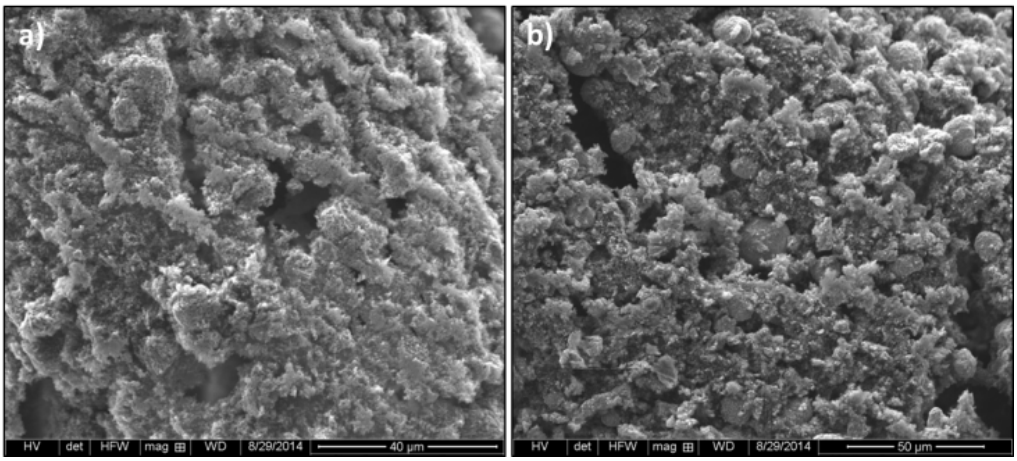

Figure 19. SEM images of the bottom side of a) Two-stage dried electrode with 40µm scale and b) Accelerated single-stage electrode with 50µm scale.

As expected, the two-stage dried sheet can be observed to have more binder (shown as the lighter regions) at the bottom of the sheet than the quickly dried sheet. Without enough time for redistribution of particles, the bottom of the single-stage electrode is

lacking in binder, which could result in delamination. Both sheets exhibited sufficient adhesion during a 1mm bend test, where the electrode is wound around a 1mm rod, thus replicating the standard spirally-wound configuration found in wound cylindrical cells.

Electrochemical Analysis

In performing the electrochemical analysis, a separate electrode sheet was created and dried, apart from the electrode sheet utilized in the examination of the drying rate to ensure that the weighing process (taking the sheet in and out of the oven) had no effects on the final electrode. The impedance spectrum for the two-stage and single-stage electrodes can be seen in Figure 20.

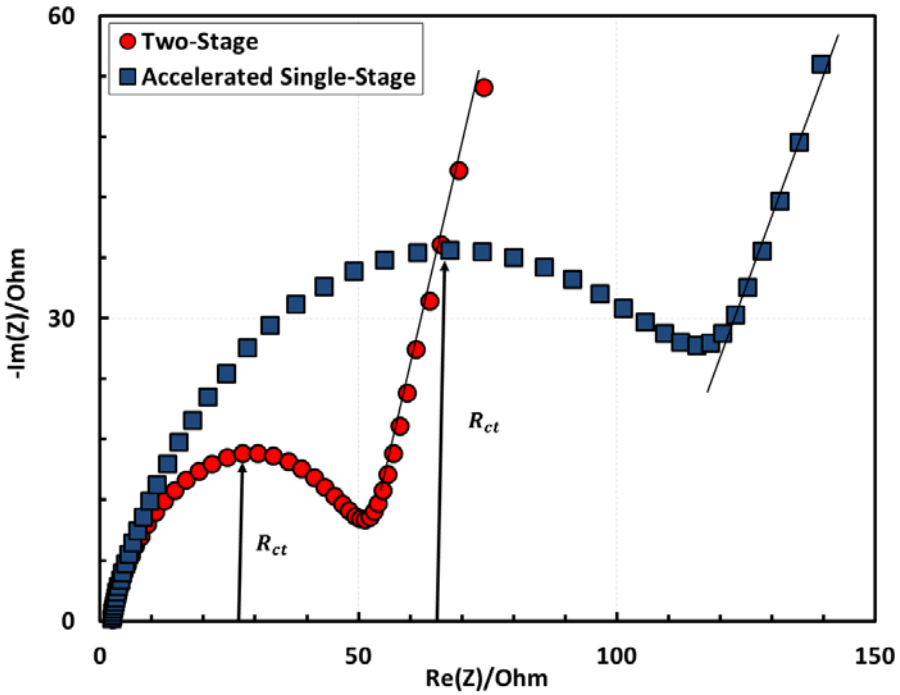

Figure 20. Electrochemical impedance spectroscopy data for each electrode sheet. Data shown is representative across multiple evaluated cells.

The high frequency intercept indicates the total ohmic resistance of the cell, which is primarily due to the electrolyte. With no differences in cell construction, the resistance shows little difference between the two cases. Moving into the lower frequency range, a single semicircle, followed by a tail can be seen for each sheet. The semicircle represents the internal resistance of the cell due to charge-transfer resistance at the electrode-electrolyte interface, current collector resistance, and resistive contributions from the porosity and conductivity of the electrode. The increase in diameter of the semicircle for the single-stage dry indicates an increase in the overall charge transfer resistance. Given that the cell composition and electrical leads are maintained constant, the differences must be due to microstructural differences between the electrodes, namely the non-uniform distribution of additive and binder. Additionally, the poor distribution of carbon would further amplify this effect throughout the electrode. With the reduced amount of binder present at the bottom of the single-stage electrode, reduced electrode adhesion is also expected, which reduces conduction between the electrode and current collector. Lastly, the tail represents the resistance associated with the diffusion of ions within the electrode[60]. Here the slope of the tail is indicative of the resistance, with an increase in slope indicating an increase in diffusion resistance. The diffusion resistance for the two-stage sheet is slightly higher than that of the single-stage sheet, likely owing to slight differences in porosity. However, this contribution towards the overall cell resistance is minimal.

To further probe the electrochemical impact of drying rate on the microstructure of the cathodes, rate and cycling performance were probed. The cycling performance of

the electrode sheets can be observed in Figure 21. The plotted data represents the average case for three coin cells constructed from each electrode sheet. At the lower rates (C/10, C/5) the single-stage and two stage electrodes have no significant difference in cell performance. As the rate is further increased, the difference in performance between the two cases rises to 2% at 1C, 4% at 2C, and 11% at 5C. As the rate of discharge increases the impact of the difference in charge transfer is apparent. As the cells are further cycled, a notable capacity drop-off is observed for the single-stage sheet, leading to capacity retention of approximately 91% for the two-stage sheet, and 78% for the single-stage.

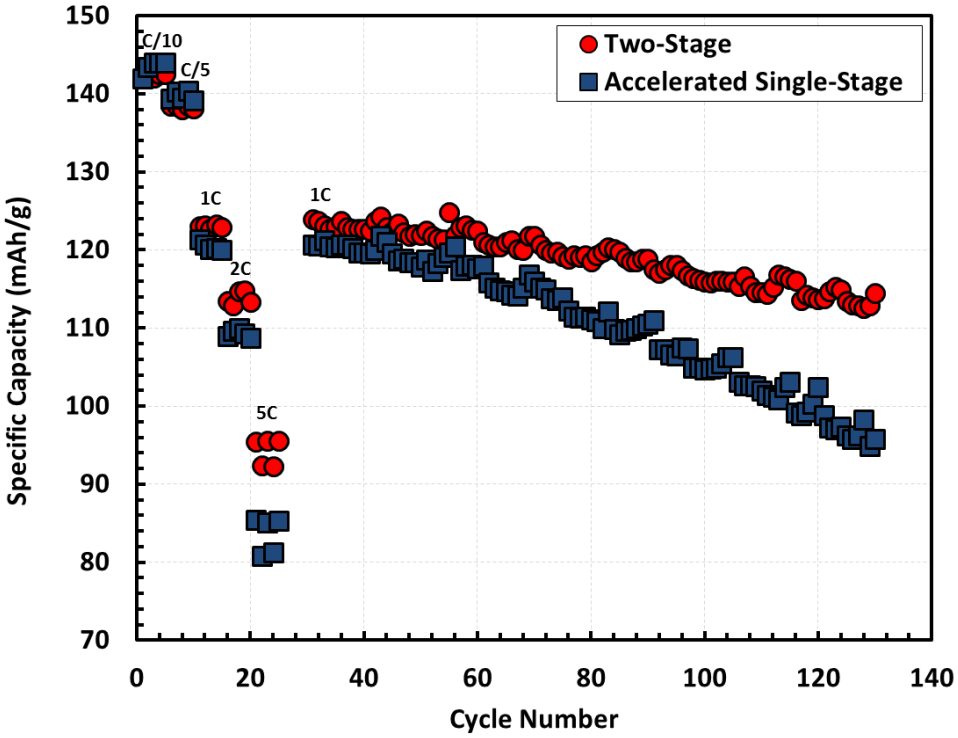

Figure 21. Specific capacity as a function of cycle number and discharge rate for coin cells made from the two-stage and single stage electrode sheets. The cycling consisted of five cycles of C/10, C/5, 1C, 2C, 5C, and 10C, followed by 100 cycles at 1C.

This reduction in capacity retention can be attributed to the difference in internal resistance as previously mentioned, along with adhesion to the current collector during cycling[61].

The discharge curves at 1C and 5C for each electrode can be seen in Figure 22. As expected, the two-stage electrode outperforms the single-stage electrode at both rates in terms of specific capacity. The IR drop (shown as the lower voltage plateau) for the single-stage electrode is larger than that of the single stage, likely due to the differences in internal resistance as previously mentioned. Thus the two-stage electrodes have a higher energy density than that of the single-stage sheet, corresponding to a 3% and 14% percent difference at rates of 1C and 5C, respectively.

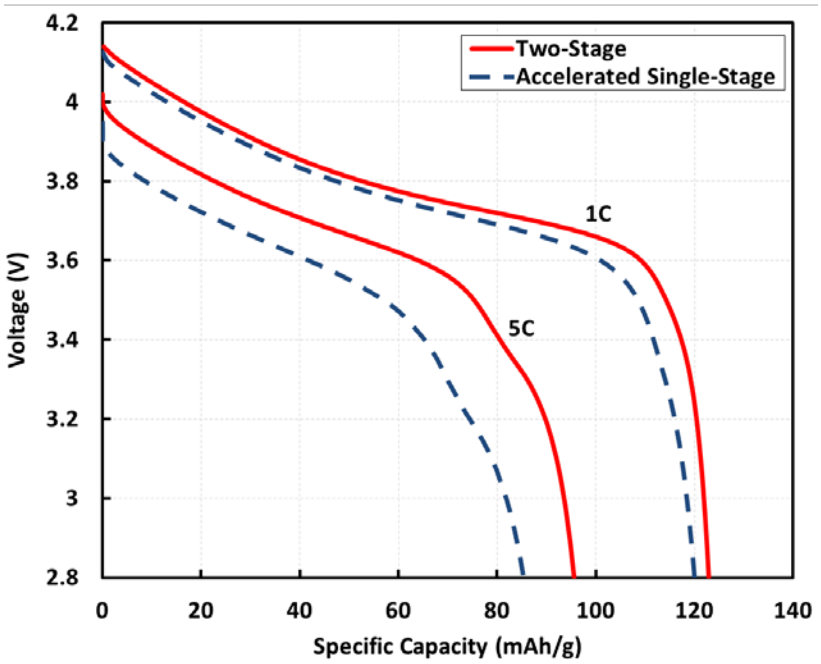

Figure 22. Discharge curves at 1C and 5C for each examined electrode, with an upper voltage limit of 4.2V and a cutoff voltage of 2.8V. Data shown is representative across multiple evaluated cells.

Physics Based Modeling of Drying

Clearly the rate of evaporation has an impact on the distribution of mobile components within the electrode, which further impacts the electrochemical performance of cells. Given a basic understanding of the drying dynamics in a simplified case, a 1-D analysis was used to identify an appropriate range of drying conditions that result in appropriate uniformity of electrodes. The migration of particles during evaporation from a thin film as shown below in Figure 23.

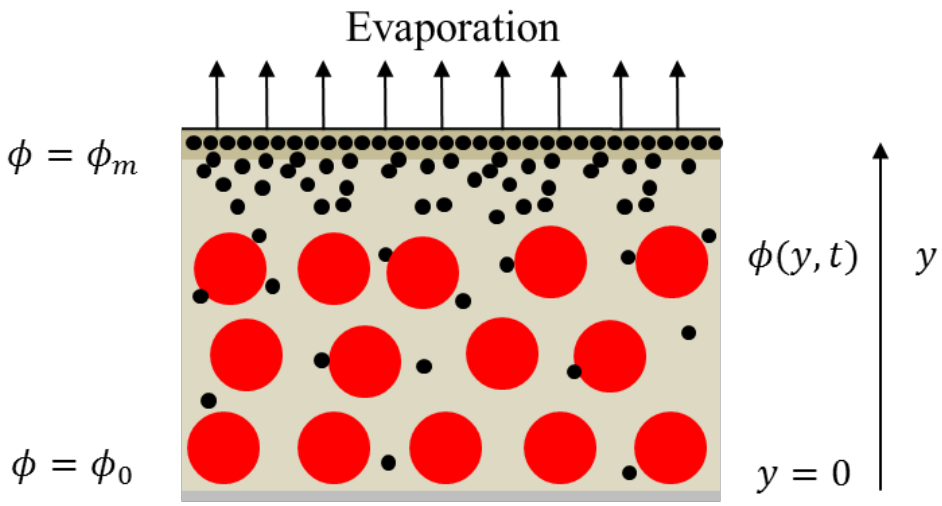

Figure 23. Sketch of evaporation from the electrode slurry.

Here the active material is represented as the large, red spheres, the black spheres represent conductive additive, the tan background represents the binder dissolved in solvent, and the dark region near the surface is a region of increased binder concentration. The top surface recedes due to evaporation, causing the binder and additive to accumulate at the surface.

The evaporation follows a convection diffusion equation, where the vertical volume fraction of particles at a given time is given as[62, 63, 64, 65, 66, 67]

$$\frac{\partial \phi}{\partial \bar{t}} = \frac{1}{Pe}\frac{\partial}{\partial \bar{y}}[K(\phi)\frac{d}{d\phi}[\phi Z(\phi)]\frac{\partial \phi}{\partial \bar{y}}]$$

where ϕ is the volume fraction, $\bar{t}$ is the dimensionless time and $\bar{y}$ is the distance from the bottom of the film. The compressibility of the dispersion $Z(\phi)$ accounts for the diffusive driving force as a result of an increase in particle chemical potential. Here it is given the functional form

$$Z(\phi) = \frac{1}{\phi_m - \phi}$$

which accounts for divergence when reaching the packing limit ϕ_m of the particles. The sedimentation coefficient $K(\phi)$ accounts for the reduction in particle diffusion coefficient as a result of inter-particle hydrodynamic interactions. To have appropriate limits at low volume fractions, the sedimentation coefficient is taken as[64, 68, 69, 70]

$$K(\phi) = (1-\phi)^{6.55}.$$

The dimensionless time and distance are scaled as a function of the film height H and the evaporation rate $\dot{E}$ are given as

$$\bar{t} = \frac{t\dot{E}}{H}$$
$$\bar{y} = \frac{y}{H}.$$

No flux conditions exists at the upper and lower boundaries of the sheet, leading to

$$\overline{y} = 0, \quad K(\phi)\frac{d}{d\phi}[\phi Z(\phi)]\frac{\partial \phi}{\partial \overline{y}},$$

$$\overline{y} = 1 - \overline{t}, \quad K(\phi)\frac{d}{d\phi}[\phi Z(\phi)]\frac{\partial \phi}{\partial \overline{y}} = Pe\phi.$$

As the drying time increases, the top layer decreases in height, as noted by the decreasing upper limit of y/H. At time t=1, the sheet will be fully dried, however the imposed limit on the upper volume fraction prevents this from ever being reached. Thus we cannot fully "dry" the sheets, merely predict the distribution of particles based upon the longest drying time achievable. Regardless, this model provides a qualitative measure of particle distribution.

In applying this analysis to electrode slurries, the slurries are assumed to be uniform, such that migration of binder due to solvent evaporation is accompanied by the migration of conductive additive that is suspended in the solution. The drying of the sheets is assumed to be uniform in the drying direction, such that the evaporation front proceeds at a constant rate across the entire electrode sheet. Active material particles are assumed to be uniformly distributed with minimal settling, due to the viscosity of the slurry. However, the size of the particles prevents redistribution following the migration of binder and additive.

The governing equation was solved using a finite element solver, at Peclet numbers of 0.1 and 1, respectively corresponding to the accelerated and two stage drying

schemes. Here the only factors that change are the temperature, solvent viscosity, and the evaporation rate. The solvent viscosity changes as a function of temperature, along with the evaporation rate, which is defined as the rate at which the upper surface of the film recedes during evaporation. Although two mobile phases are present, the radius of the Super-C65 was utilized in this analysis, as the additive will likely be the limiting factor in mobility. Super-C65 carbon black tends to aggregate, with a primary particle size of approximately 100nm[71]. The initial volume fraction of binder and additive was evaluated to be approximately 20% in the electrode slurry. The upper limit was chosen as 64%, corresponding to the maximum volume fraction for random close packing[72, 73]. The volume fraction distribution for $Pe = 1$ is shown below in Figure 24.

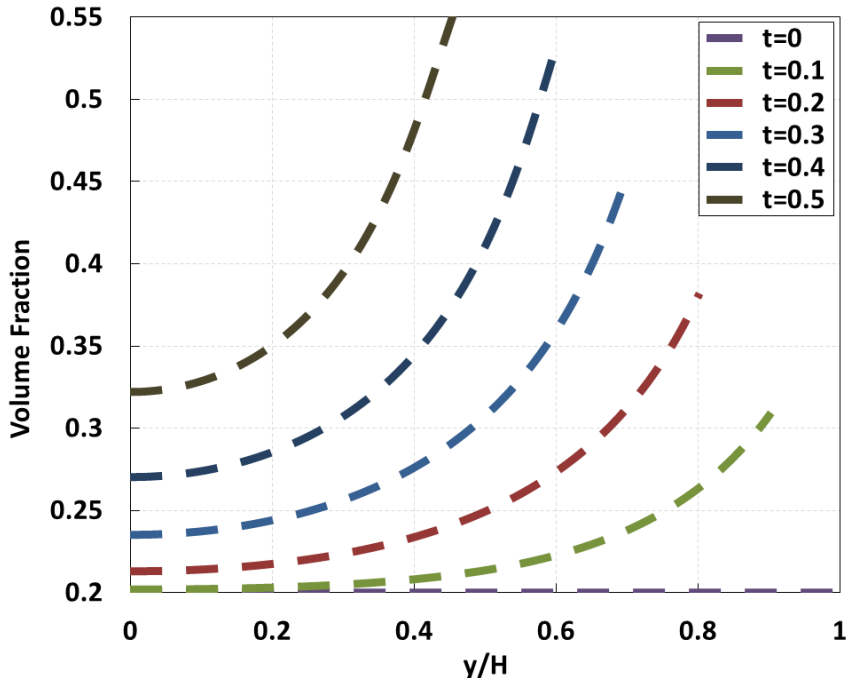

Figure 24. Volume fraction distribution of binder/conductive additive as a function of drying time for the accelerated drying rate, where $Pe \approx 1$.

The evolution of the particle distribution can be seen from t=0 to t=0.5, the point where drying is 50% complete. A t=0, the slurry is fully wet, with the volume fraction of the binder/additive constant at 20%. Here the sheet remains at the initial casting height, as noted by the range of volume fraction data. As the time increases to t=0.1, the solvent begins to evaporate from the surface, leaving an increased concentration of binder/additive on the surface of decreasing height. As time increases further, the vertical accumulation of components becomes more apparent. A measure of redistribution occurs, as noted by the increase in volume fraction at the bottom of the sheet. However, a large gradient still exists within the sheet, where the majority of the binder/additive is in the upper half of the sheet. This additionally indicates a reduction in porosity towards the surfaces of the sheet, due to the increased content of binder/additive. The volume fraction distribution for Pe=1 is shown below in Figure 25.

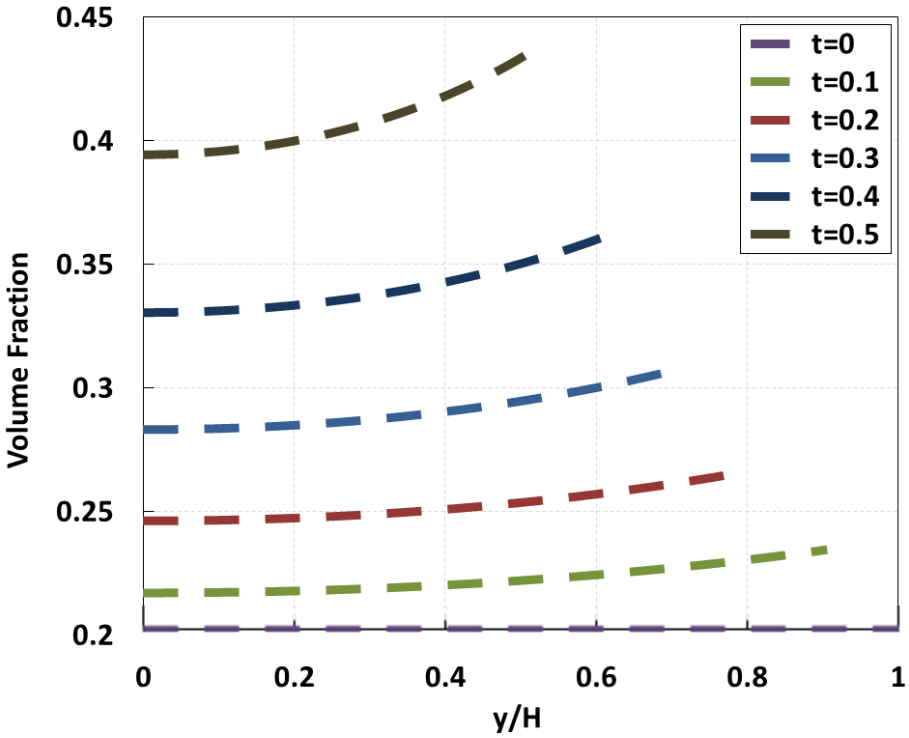

Figure 25. Volume fraction distribution of binder/conductive additive as a function of drying time for the accelerated drying rate, where Pe≈0.1.

The evolution of the volume fraction distribution follows the same trend found for Pe=1, whereby the thickness of the sheet decreases as evaporation occurs, and the volume fraction of additive/binder increases towards the top of the sheet. However, whereas the diffusion rate was too slow for the case of Pe=1, here it is ample enough to allow for the redistribution of electrode components during drying, preventing the sharp increase in volume fraction shown for the case where Pe=1. Here the particle distributions are much more uniform at every given time as compared to the quickly dried sheet. The volume fraction at the bottom of the sheet increases with time, as the particles have enough time to diffuse through the sheet as opposed to remaining near the

surface. Given the relative performance of the two cases, it is clear that a more uniform distribution of conductive additive and binder is needed in order to maximize the potential of an electrode with a given composition.

In order to broaden the results of this study and create an guideline for the optimization of electrode microstructures during the drying stage, the previous analysis was extended to a range of Peclet numbers (0.1, 0.5, 1, and 2) and a range of initial volume fractions (0.05, 0.1, 0.15, and 0.2) in order to account for varying film characteristics and volume fraction of mobile constituents. In a practical lab setting, the primary factors effecting the Peclet number are the ambient temperature, the solvent viscosity, particle radius and film height. Alteration of these quantities will increase or decrease the Peclet number. Changes to the volume fraction can be easily achieved by simply altering the desired weight percentages of components in the final, dried electrode. Particle size is altered by simply choosing a different additive type, are taking steps – such as milling – to reduce the particle size of an existing additive. Casting height will have a direct impact on the initial and final film height, although the final height will also be impacted by the composition of the slurry.

In analyzing the volume fraction distributions for these cases, a factor representing the normalized deviation of volume fraction from the average volume fraction for the semi-dried sheets was utilized. This factor is defined as the standard deviation of the volume fraction divided by the average volume fraction, at t=0.5. As the distribution of particles follows an increase in volume fraction towards the top of the

sheet, an increase in the normalized deviation indicates a higher degree of vertical accumulation. The plotted results can be seen in Figure 26.

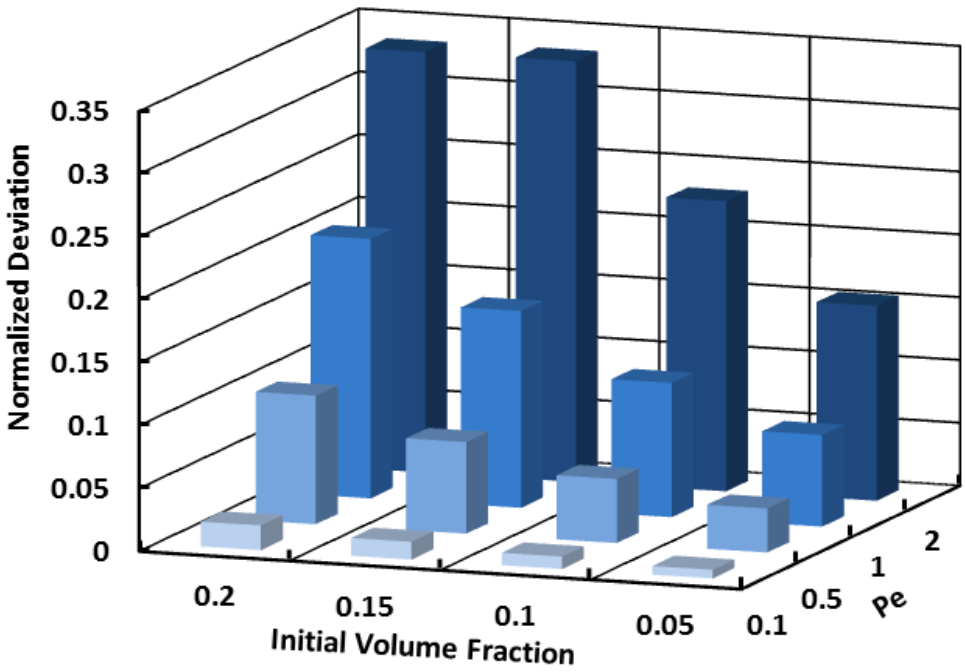

Figure 26. Normalized deviation of binder/additive volume fraction as a function of Peclet number and initial volume fraction of carbon/additive in the electrode slurry.

For a constant initial volume fraction, the normalized deviation of volume fraction increases up to between 15% and 35%. Regardless of the content, vertical accumulation will still occur with the final amount of additive present at the top surface of the sheet only limited by the total amount of binder/additive present in the sheet. However, at the lower volume fraction (0.05 and 0.1) the normalized distribution is less than that of the 15% and 20% initial volume fraction cases. Essentially, the larger the concentration of the binder/additive in the initial slurry and the higher the Peclet number,

the greater degree of vertical accumulation will occur. Thus in order to maximize the uniformity of electrode sheets with given mobile constituents, the rate of evaporation and the initial film height must be controlled. For example, a thicker sheet will need to dry at a lower rate than a thinner sheet with the same composition in order to maintain a constant Peclet number and reduce the non-uniformity of the electrode.

CHAPTER IV

EFFECT OF CALENDERING

An optional post-processing step, known as calendering, can additionally be applied to the dried and punched electrodes, prior to constructing the coin cell. Calendering is the process of compressing an electrode to reduce its porosity. Thus the energy density of the electrodes in increased, and the performance is typically improved, due to better contact between components and improved electrode adhesion to the current collector[52, 74, 75, 76, 77, 78]. However, it is possible during the compression process that the effects of particle distribution can be offset, as particles are forced closer together.

Traditionally electrode sheets are calendered via the usage of a rolling machine, where a cast electrode sheet is rolled through two metal cylinders with a pre-set gap width. In addition to being a good post-processing step, calendering can also help to gauge the adhesion of cast electrode sheets. Generally speaking, if the electrode peels or flakes from the current collector whilst calendering, then the cell will likely have poor performance, especially during cycling. Although the traditional method of rolling has the added benefit of allowing for the calendering of entire electrode sheets – the main reason this method is utilized in industry – the equipment itself is useful only in this application. Thus a multi-purpose lab-press is used to calender punched out electrode on

a singular basis. Here the electrode is placed between two stainless steel spacers, and pressure of 4MPa is applied, as shown in Figure 27.

Figure 27. Lab press shown with electrode sample on stainless steel spacer.

The calendered electrode can be seen in Figure 28, next to an uncalendered electrode.

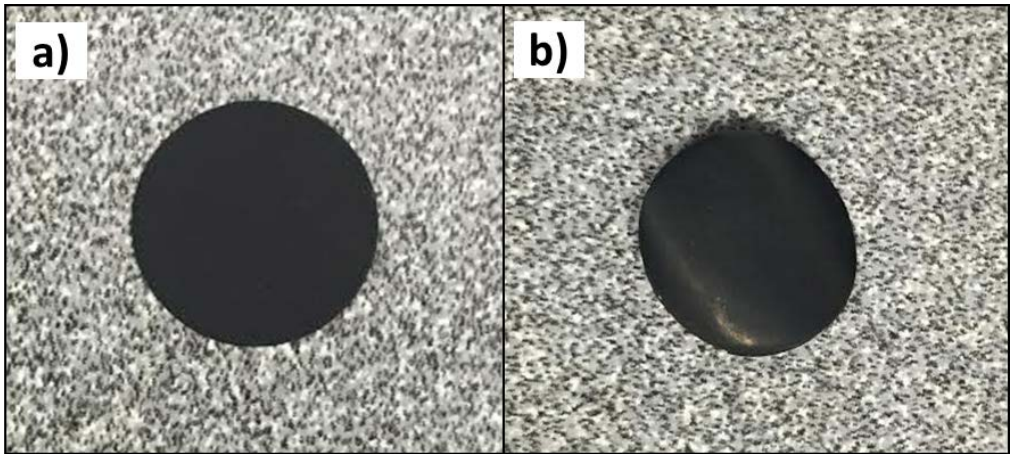

Figure 28. Punched out uncalendered (a) and calendered (b) electrodes.

A pressure of 4MPa was arbitrarily chosen after determining that this pressure yielded optimal results in terms of performance on a separate benchmark study. The reasoning for this optimal pressure is directly linked to the porosity of the electrode as a function of calendering pressure, and is beyond the scope of this current work.

SEM images of the calendered electrode for the two-stage and single-stage dry can be seen below in Figure 29.

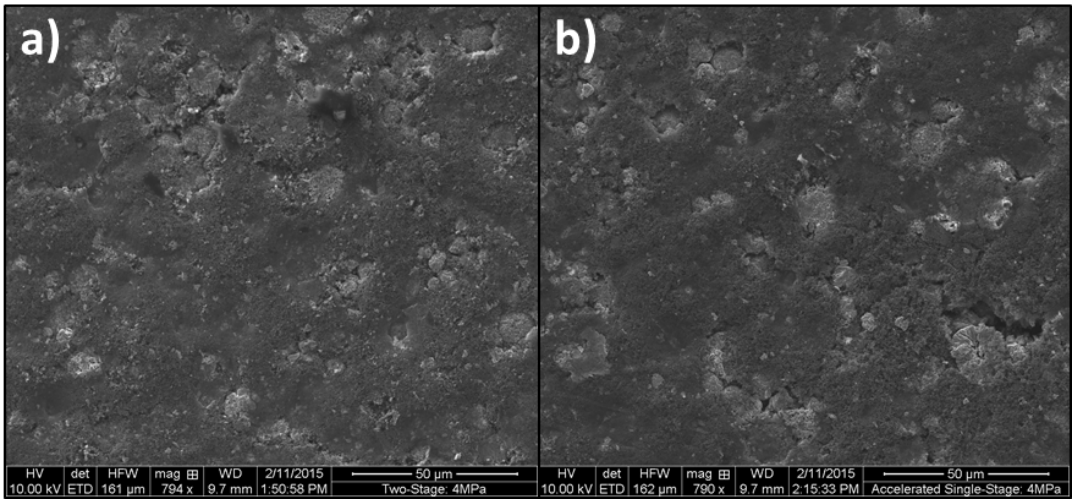

Figure 29. SEM images of a) Two-stage dried, calendered electrode sheet zoomed out with 50µm scale and b) Accelerated single-stage, calendered electrode sheet zoomed out with 50µm scale.

Immediately noticeable is the degree of compaction, as compared to the uncalendered samples. In addition to pushing the components closer together, noticeable cracking of the active material particles occurred in both cases, as shown in Figure 30.

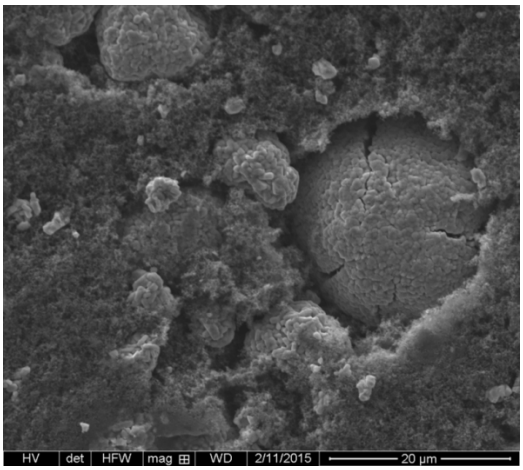

Figure 30. SEM image with cracking NMC particle with a 20µm scale.

The electrochemical impact of these microstructural changes can be observed looking at the electrochemical impedance spectrum of the electrodes. Figure 31 displays the EIS data for the two calendered electrodes, compared alongside with the EIS spectrum for the uncalendered electrodes.

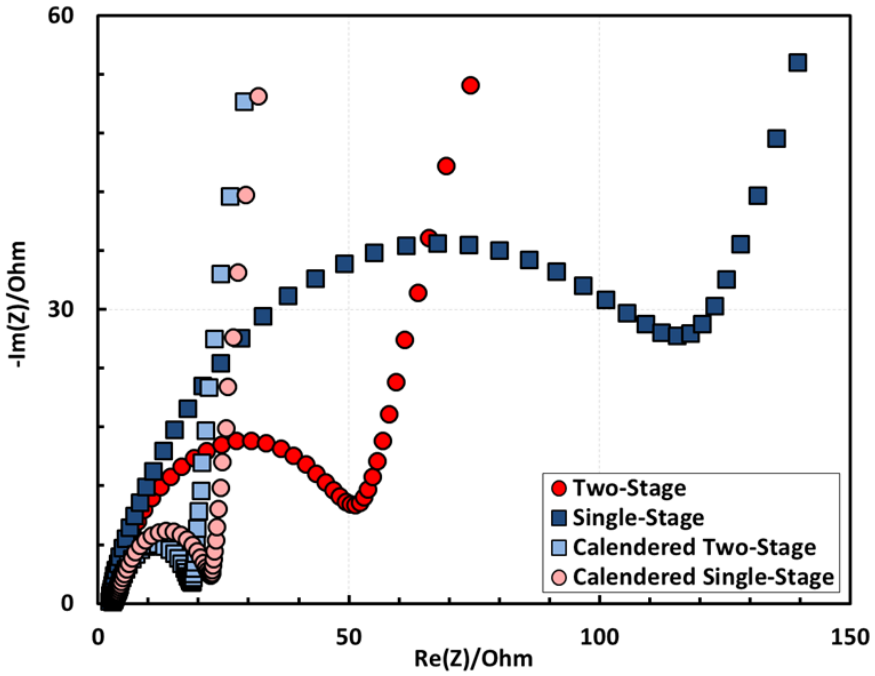

Figure 31. Electrochemical impedance spectroscopy data for calendered and uncalendered electrode sheet for each drying speed. Data shown is representative across multiple evaluated cells.

Immediately noticeable is the significantly smaller semicircle present for the calendered cases, which indicates both a lower charge transfer resistance and electrode/current collector interface impedance. Amongst themselves, the two-stage sheet still exhibits a

lower internal resistance as compared to the single-stage dry. The cycling performance of the calendered electrodes can be seen in Figure 32.

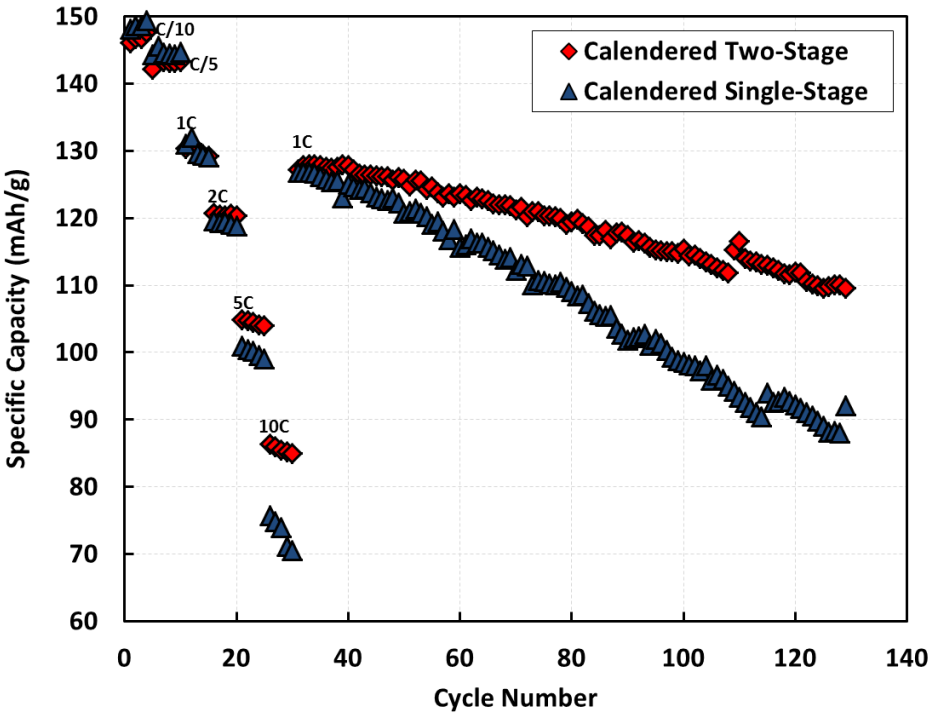

Figure 32. Specific capacity as a function of cycle number and discharge rate for coin cells made from the calendered two-stage and single stage electrode sheets. The cycling consisted of five cycles of C/10, C/5, 1C, 2C, 5C, and 10C, followed by 100 cycles at 1C.

Compared to the non-calendered samples, the calendered sheets display increases in capacity at each rate. However, these sheets exhibit capacity retentions of 85% for the slowly dried case and 68% for the quickly dried sheet, while the uncalendered sheets had retentions of 91% and 78%, respectively. The difference between the two calendered cases is likely linked to the previous analysis of particle distribution. The increase in

capacity fade as compared to the uncalendered sheet can be linked to the cracking of NMC particles as a result of the compression. During cycling cracks can form in the active material particles that hinder performance. By starting this cycling with cracks already established, a greater degree of crack propagation will likely occur, thus reducing capacity retention[79, 80].

CHAPTER V

SUMMARY AND FUTURE RECOMMENDATIONS

The influence of evaporation rate on microstructure formation in LIB electrodes has been explored through an experimental approach coupled with 1-D analysis. For accelerated electrode drying, a non-uniform distribution of binder and conductive additive develops that results in poor cycleability and reduced electrochemical performance. The theoretical distribution indicates that vertical accumulation of additive and binder will occur when the drying rate is too high, as denoted by the Peclet number for the given drying conditions. With calendering, the performance of cells is greatly improved, but the effects do not negate the impact of microstructure formation during drying. Taken as a whole, the results of this work can be generalized and used to optimize the fabrication of LIB electrodes with a number of different chemistries.

Further studies could look into further optimizing the drying time of LIB electrodes. In this case an optimal two-stage dry was utilized, however experimental time constraints limited the number of trials that could be performed. Additionally, different drying schemes could be utilized that incorporate IR or UV light.

The development of a model specifically tailored to the multi-component nature of an LIB electrode slurry needs to be developed that will enable better understanding of the drying dynamics present. Particle interactions will likely play a large role in the migration of mobile constituents[81], a factor that is not captured with the model presented herein. Furthermore, such a model could be used to accurately predict the volumetric

distribution of components on an individual basis, which could be instrumental in elucidating the full impact of particle distribution on critical electrode properties, such as conductivity, porosity, and tortuosity, to name a few.

Lastly, any work of this nature should be experimentally verified. Although evidence suggests the feasibility of the utilized 1-D analysis, XRT can be utilized to map out the volume fraction of an entire electrode. Although there was not sufficient time to include this analysis in this work, further research is pending.

REFERENCES

1. Wagner, R.; Preschitschek, N.; Passerini, S.; Leker, J.; Winter, M. Current research trends and prospects among the various materials and designs used in lithium-based batteries. *Journal of Applied Electrochemistry* **2013,** *43* (5), 481-496.

2. Whittingham, M. S. Lithium batteries and cathode materials. *Chemical Reviews* **2004,** *104* (10), 4271-301.

3. Ellis, B. L.; Lee, K. T.; Nazar, L. F. Positive Electrode Materials for Li-Ion and Li-Batteries. *Chemistry of Materials* **2010,** *22* (3), 691-714.

4. Tarascon, J. M.; Armand, M. Issues and challenges facing rechargeable lithium batteries. *Nature* **2001,** *414* (6861), 359-67.

5. Lu, L. G.; Han, X. B.; Li, J. Q.; Hua, J. F.; Ouyang, M. G. A review on the key issues for lithium-ion battery management in electric vehicles. *Journal of Power Sources* **2013,** *226*, 272-288.

6. Smith, K.; Wang, C. Y. Power and thermal characterization of a lithium-ion battery pack for hybrid-electric vehicles. *Journal of Power Sources* **2006,** *160* (1), 662-673.

7. Dunn, B.; Kamath, H.; Tarascon, J. M. Electrical energy storage for the grid: a battery of choices. *Science* **2011,** *334* (6058), 928-35.

8. Elul, S.; Cohen, Y.; Aurbach, D. The influence of geometry in 2D simulation on the charge/discharge processes in Li-ion batteries. *Journal of Electroanalytical Chemistry* **2012,** *682*, 53-65.

9. Buqa, H.; Goers, D.; Holzapfel, M.; Spahr, M. E.; Novak, P. High rate capability of graphite negative electrodes for lithium-ion batteries. *Journal of the Electrochemical Society* **2005,** *152* (2), A474-A481.

10. Chen, Y. H.; Wang, C. W.; Zhang, X.; Sastry, A. M. Porous cathode optimization for lithium cells: Ionic and electronic conductivity, capacity, and selection of materials. *Journal of Power Sources* **2010,** *195* (9), 2851-2862.

11. Arora, P.; Doyle, M.; Gozdz, A. S.; White, R. E.; Newman, J. Comparison between computer simulations and experimental data for high-rate discharges of plastic lithium-ion batteries. *Journal of Power Sources* **2000,** *88* (2), 12.

12. Dillon, S. J.; Sun, K. Microstructural design considerations for Li-ion battery systems. *Curr Opin Solid St M* **2012,** *16* (4), 153-162.

13. Zheng, H.; Li, J.; Song, X.; Liu, G.; Battaglia, V. S. A comprehensive understanding of electrode thickness effects on the electrochemical performance of Li-ion battery cathodes. *Electrochimica Acta* **2012,** *71*, 7.

14. Bates, J. B.; Dudney, N. J.; Neudecker, B.; Ueda, A.; Evans, C. D. Thin-film lithium and lithium-ion batteries. *Solid State Ionics* **2000,** *135* (1-4), 33-45.

15. Kim, J. K.; Cheruvally, G.; Choi, J. W.; Ahn, J. H.; Lee, S. H.; Choi, D. S.; Song, C. E. Effect of radical polymer cathode thickness on the electrochemical performance of organic radical battery. *Solid State Ionics* **2007,** *178* (27-28), 1546-1551.

16. Dudney, N. J.; Jang, Y. I. Analysis of thin-film lithium batteries with cathodes of 50 nm to 4 mu m thick LiCoO2. *Journal of Power Sources* **2003,** *119*, 300-304.

17. Chen, Y. H.; Wang, C. W.; Zhang, X.; Sastry, A. M. Porous cathode optimization for lithium cells: Ionic and electronic conductivity, capacity, and selectrion of materials. *Journal of Power Sources* **2010,** *195*, 11.

18. Xiang, X.; Li, X.; Li, W. Preparation and characterization of size-uniform Li[Li0.131Ni0.304Mn0.565]O2 particles as cathode materials for high energy lithium ion battery. *Journal of Power Sources* **2013,** *230*, 6.

19. Drezen, T.; Kwon, N. H.; Bowen, P.; Teerlinck, I.; Isono, M.; Exnar, I. Effect of particle size on LiMnPO4 cathodes. *Journal of Power Sources* **2007,** *174* (2), 949-953.

20. Delacourt, C.; Poizot, P.; Levasseur, S.; Masquelier, C. Size effects on carbon-free LiFePO4 powders. *Electrochem Solid St* **2006,** *9* (7), A352-A355.

21. Jiang, C. H.; Wei, M. D.; Qi, Z. M.; Kudo, T.; Honma, I.; Zhou, H. S. Particle size dependence of the lithium storage capability and high rate performance of nanocrystalline anatase TiO2 electrode. *Journal of Power Sources* **2007,** *166* (1), 239-243.

22. Kwon, N. H. The effecto of carbon morphology on the LiCoO2 cathode of lithium ion batteries. *Solid State Sciences* **2013,** *21*, 6.

23. Wang, G. P.; Zhang, Q. T.; Yu, Z. L.; Qu, M. Z. The effect of different kinds of nano-carbon conductive additives in lithium ion batteries on the resistance and electrochemical behavior of the LiCoO2 composite cathodes. *Solid State Ionics* **2008,** *179* (7-8), 263-268.

24. Chen, Y. H.; Wang, C. W.; Liu, G.; Song, X. Y.; Battaglia, V. S.; Sastry, A. M. Selection of conductive additives in Li-ion battery cathodes - A numerical study. *Journal of the Electrochemical Society* **2007,** *154* (10), A978-A986.

25. Ahn, S.; Kim, Y.; Kim, K. J.; Kim, T. H.; Lee, H.; Kim, M. H. Development of high capacity, high rate lithium ion batteries utilizing metal fiber conductive additives. *Journal of Power Sources* **1999,** *81*, 896-901.

26. Zaghib, K.; Shim, J.; Guerfi, A.; Charest, P.; Striebel, K. A. Effect of carbon source as additives in LiFePO4 as positive electrode for lithium-ion batteries. *Electrochem Solid St* **2005,** *8* (4), A207-A210.

27. Jin, B.; Gu, H. B.; Kim, K. W. Effect of different conductive additives on charge/discharge properties of LiCoPO4/Li batteries. *J Solid State Electr* **2008,** *12* (2), 105-111.

28. Liu, G.; Zheng, H.; Song, X.; Battaglia, V. S. Particles and Polymer Binder Interaction: A Controlling Factor in Lithium-Ion Electrode Performance. *Journal of the Electrochemical Society* **2012,** *159* (3), A214-A221.

29. Shim, J.; Striebel, K. A.; Cairns, E. J. The lithium/sulfur rechargeable cell - Effects of electrode composition and solvent on cell performance. *Journal of the Electrochemical Society* **2002,** *149* (10), A1321-A1325.

30. Harris, S. J.; Lu, P. Effects of Inhomogeneities-Nanoscale to Mesoscale-on the Durability of Li-Ion Batteries. *J Phys Chem C* **2013,** *117* (13), 6481-6492.

31. Yabuuchi, N.; Ohzuku, T. Electrochemical behaviors of LiCo1/3Ni1/3Mn1/3O2 in lithium batteries at elevated temperatures. *Journal of Power Sources* **2005,** *146* (1-2), 636-639.

32. Marks, T.; Trussler, S.; Smith, A. J.; Xiong, D. J.; Dahn, J. R. A Guide to Li-Ion Coin-Cell Electrode Making for Academic Researchers. *Journal of the Electrochemical Society* **2011,** *158* (1), A51-A57.

33. Kayyar, A.; Huang, J.; Samiee, M.; Luo, J. Construction and testing of coin cells of lithium ion batteries. *Journal of Visualized Experiments : JoVE* **2012,** (66), e4104.

34. Zheng, H.; Liu, G.; Crawford, S.; Battaglia, V. S. Fabrication Procedure for Lithium-ion Rechargeable Coin Cells. Laboratory, L. B. N., Ed.: Berkeley, California, 2010.

35. Li, C. C.; Wang, Y. W. Binder Distributions in Water-Based and Organic-Based LiCoO2 Electrode Sheets and Their Effects on Cell Performance. *Journal of the Electrochemical Society* **2011,** *158* (12), A1361-A1370.

36. Liu, Z. X.; Mukherjee, P. P. Microstructure Evolution in Lithium-Ion Battery Electrode Processing. *Journal of the Electrochemical Society* **2014,** *161* (8), E3248-E3258.

37. Carreras, E. S.; Chabert, F.; Dunstan, D. E.; Franks, G. V. Avoiding "mud" cracks during drying of thin films from aqueous colloidal suspensions. *Journal of Colloid and Interface Science* **2007,** *313* (1), 160-168.

38. Xu, P.; Mujumdar, A. S.; Yu, B. Drying-Induced Cracks in Thin Film Fabricated from Colloidal Dispersions. *Drying Technology* **2009,** *27* (5), 636-652.

39. Routh, A. F. Drying of thin colloidal films. *Reports on Progress in Physics. Physical Society* **2013,** *76* (4), 046603.

40. Scherer, G. W. Theory of Drying. *J Am Ceram Soc* **1990,** *73* (1), 3-14.

41. Wedin, P.; Martinez, C. J.; Lewis, J. A.; Daicic, J.; Bergstrom, L. Stress development during drying of calcium carbonate suspensions containing carboxymethylcellulose and latex particles. *Journal of Colloid and Interface Science* **2004,** *272* (1), 1-9.

42. Holl, Y.; Keddie, J. L.; McDonald, P.; Winnik, W. Drying Modes of Polymer Colloids. *American Chemical Society* **2001**, 24.

43. Sheetz, D. P. Formation of Films by Drying of Latex. *J Appl Polym Sci* **1965,** *9* (11), 3759-&.

44. Routh, A. F.; Russel, W. B. Horizontal drying fronts during solvent evaporation from latex films. *Aiche J* **1998,** *44* (9), 2088-2098.

45. Lee, W. P.; Routh, A. F. Why do drying films crack? *Langmuir* **2004,** *20* (23), 9885-9888.

46. Aurbach, D.; Gamolsky, K.; Markovsky, B.; Gofer, Y.; Schmidt, M.; Heider, U. On the use of vinylene carbonate (VC) electrolyte solutions for Li-ion as an additive to batteries. *Electrochimica Acta* **2002,** *47* (9), 1423-1439.

47. Jouanneau, S.; MacNeil, D. D.; Lu, Z.; Beattie, S. D.; Murphy, G.; Dahn, J. R. Morphology and Safety of Li[NixCo1-2xMnx]O-2 (0 <= x <= 1/2). *Journal of the Electrochemical Society* **2003,** *150* (10), A1299-A1304.

48. Belharouak, I.; Sun, Y. K.; Liu, J.; Amine, K. Li(Ni1/3Co1/3Mn1/3)O-2 as a suitable cathode for high power applications. *Journal of Power Sources* **2003,** *123* (2), 247-252.

49. Johnson, C. S.; Li, N. C.; Lefief, C.; Thackeray, M. M. Anomalous capacity and cycling stability of xLi(2)MnO(3)center dot(1-x)LiMO2 electrodes (M = Mn, Ni, Co) in lithium batteries at 50 degrees C. *Electrochemistry Communications* **2007,** *9* (4), 787-795.

50. Shaju, K. M.; Bruce, P. G. Macroporous Li(Ni1/3Co1/3Mn1/3)O-2: A high-power and high-energy cathode for rechargeable lithium batteries. *Adv Mater* **2006,** *18* (17), 2330-+.

51. La Mantia, F.; Rosciano, F.; Tran, N.; Novak, P. Quantification of Oxygen Loss from Li(1+x)(Ni(1/3)Mn(1/3)Co(1/3))(1-x)O(2) at High Potentials by Differential Electrochemical Mass Spectrometry. *Journal of the Electrochemical Society* **2009,** *156* (11), A823-A827.

52. Zheng, H.; Tan, L.; Liu, G.; Song, X.; Battaglia, V. S. Calendering effects on the physical and electrochemical properties of Li[Ni1/3Mn1/3Co1/3]O2 cathode. *Journal of Power Sources* **2012,** *208*, 5.

53. Vijayaraghavan, B.; Ely, D. R.; Chiang, Y. M.; Garcia-Garcia, R.; Garcia, R. E. An Analytical Method to Determine Tortuosity in Rechargeable Battery Electrodes. *Journal of the Electrochemical Society* **2012,** *159* (5), A548-A552.

54. Thorat, I. V.; Stephenson, D. E.; Zacharias, N. A.; Zaghib, K.; Harb, J. N.; Wheeler, D. R. Quantifying tortuosity in porous Li-ion battery materials. *Journal of Power Sources* **2009,** *188* (2), 592-600.

55. Shearing, P. R.; Howard, L. E.; Jorgensen, P. S.; Brandon, N. P.; Harris, S. J. Characterization of the 3-dimensional microstructure of a graphite negative electrode from a Li-ion battery. *Electrochemistry Communications* **2010,** *12* (3), 374-377.

56. Mukherjee, P. P.; Pannala, S.; Turner, J. A. Modeling and Simulation of Battery Systems. Wiley-VCH Verlag GmbH & Co. KGaA: Weinheim, Germany, 2011.

57. Ramadesigan, V.; Northrop, P. W. C.; De, S.; Santhanagopalan, S.; Braatz, R. D.; Subramanian, V. R. Modeling and Simulation of Lithium-Ion Batteries from a Systems Engineering Perspective. *Journal of the Electrochemistry Society* **2012,** *159*, 14.

58. Ender, M.; Joos, J.; Carraro, T.; Ivers-Tiffee, E. Three-dimensional reconstruction of a composite cathode for lithium-ion cells. *Electrochemistry Communications* **2011,** *13* (2), 166-168.

59. Liu, G.; Zheng, H.; Kim, S.; Deng, Y.; Minor, A. M.; Song, X.; Battaglia, V. S. Effects of Various Conductive Additive and Polymeric Binder Contents on the Performance of a Lithium-Ion Composite Cathode. *Journal of the Electrochemical Society* **2008,** *155* (12), A887-A892.

60. Levi, M. D.; Aurbach, D. Diffusion coefficients of lithium ions during intercalation into graphite derived from the simultaneous measurements and modeling of electrochemical impedance and potentiostatic intermittent titration characteristics of thin graphite electrodes. *J Phys Chem B* **1997,** *101* (23), 4641-4647.

61. Arora, P.; White, R. E.; Doyle, M. Capacity fade mechanisms and side reactions in lithium-ion batteries. *Journal of the Electrochemical Society* **1998,** *145* (10), 3647-3667.

62. Routh, A. F.; Zimmerman, W. B. Distribution of particles during solvent evaporation from films. *Chemical Engineering Science* **2004,** *59* (14), 2961-2968.

63. Keddie, J. L.; Routh, A. F. Drying of Latex Films. In *Fundamentals of Latex Film Formation*; Springer Netherlands, 2010, pp 95-120.

64. Russel, W. B.; Saville, W. B.; Schowalter, D. A. *Colloidal Dispersions*; Cambridge University Press: Cambridge, 1995.

65. Shimmin, R. G.; DiMauro, A. J.; Braun, P. V. Slow vertical deposition of colloidal crystals: A Langmuir-Blodgett process? *Langmuir* **2006,** *22* (15), 6507-6513.

66. Brown, L. A.; Zukoski, C. F.; White, L. R. Consolidation during drying of aggregated suspensions. *Aiche J* **2002,** *48* (3), 492-502.

67. Brown, L. A.; Zukoski, C. F. Experimental tests of two-phase fluid model of drying consolidation. *Aiche J* **2003,** *49* (2), 362-372.

68. Cairns, R. J. R.; Vanmegen, W.; Ottewill, R. H. A Comparison between Theoretically Computed and Experimentally Measured Pressures for Interacting Sterically Stabilized Particles. *Journal of Colloid and Interface Science* **1981,** *79* (2), 511-517.

69. Batchelo.Gk. Sedimentation in a Dilute Dispersion of Spheres. *J Fluid Mech* **1972,** *52* (Mar28), 245-&.

70. Maude, A. D.; Whitmore, R. L. A Generalized Theory of Sedimentation. *Brit J Appl Phys* **1958,** *9* (12), 477-482.

71. Kwon, N. H. The effect of carbon morphology on the LiCoO2 cathode of lithium ion batteries. *Solid State Sciences* **2013,** *21*, 59-65.

72. Song, C.; Wang, P.; Makse, H. A. A phase diagram for jammed matter. *Nature* **2008,** *453* (7195), 629-632.

73. Aste, T.; Coniglio, A. Cell theory for liquid solids and glasses: From local packing configurations to global complex behaviors. *Europhys Lett* **2004,** *67* (2), 165-171.

74. Ebner, M.; Chung, D.-W.; Garcia, R. E.; Wood, V. Tortuosity Anisotrophy in Lithium-Ion Battery Electrodes. *Advanced Energy Materials* **2013**.

75. Bommel, A. v.; Divigalpitiya, R. Effect of Calendering on LiFePO4 Electrodes. *Journal of the Electrochemical Society* **2012,** *159*, 4.

76. Zheng, H.; Liu, G.; Song, X.; Ridgway, P.; Xun, S.; Battaglia, V. S. Cathode Performance as a Function of Inactive Material and Void Fraction. *Journal of the Electrochemical Society* **2010,** *157* (10), 6.

77. Kim, C.-S.; Guerfi, A.; Hovington, P.; Trottier, J.; Gagnon, C.; Barray, F.; Vijh, A.; Armand, M.; Zaghib, K. Importance of open pore structures with mechanical integrity in designing the cathode electrode for lithium–sulfur batteries. *Journal of Power Sources* **2013,** *241*, 5.

78. Lu, W. Q.; Jansen, A.; Dees, D.; Nelson, P.; Veselka, N. R.; Henriksen, G. High-energy electrode investigation for plug-in hybrid electric vehicles. *Journal of Power Sources* **2011,** *196* (3), 1537-1540.

79. Chen, C. F.; Barai, P.; Mukherjee, P. P. Diffusion Induced Damage and Impedance Response in Lithium-Ion Battery Electrodes. *Journal of the Electrochemical Society* **2014,** *161* (14), A2138-A2152.

80. Barai, P.; Mukherjee, P. P. Stochastic Analysis of Diffusion Induced Damage in Lithium-Ion Battery Electrodes. *Journal of the Electrochemical Society* **2013,** *160* (6), A955-A967.

81. Zhu, M.; Park, J.; Sastry, A. M. Particle Interaction and Aggregation in Cathode Material of Li-Ion Batteries: A Numerical Study. *Journal of the Electrochemical Society* **2011,** *158* (10), A1155-A1159.